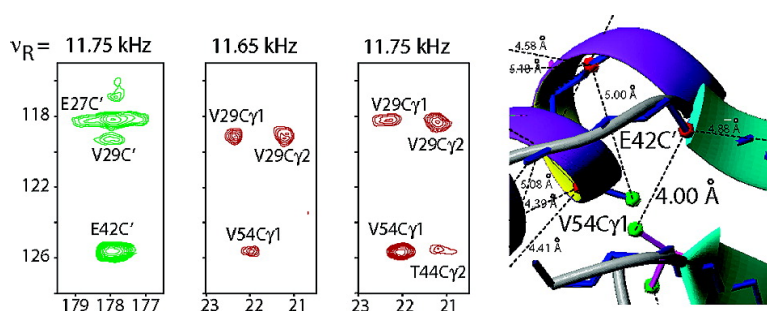Article

Dipolar Chemical Shift Correlation Spectroscopy for Homonuclear Carbon Distance Measurements in Proteins in the Solid State: Application to Structure Determination and Refinement

Xiaohu Peng, David Libich, Rafal Janik, George Harauz, and Vladimir Ladizhansky

More About This Article

Additional resources and features associated with this article are available within the HTML version:

- Supporting Information
- Links to the 4 articles that cite this article, as of the time of this article download
- Access to high resolution figures
- Links to articles and content related to this article
- Copyright permission to reproduce figures and/or text from this article

View the Full Text HTML

Dipolar Chemical Shift Correlation Spectroscopy for Homonuclear Carbon Distance Measurements in Proteins in the Solid State: Application to Structure Determination and Refinement

Xiaohu Peng,[†,§] David Libich,[‡,§] Rafal Janik,[†,§] George Harauz,[‡,§] and
Vladimir Ladizhansky*,[†,§]

*Department of Physics, Department of Molecular and Cellular Biology, and Biophysics
Interdepartmental Group, University of Guelph, 50 Stone Road East, Guelph,
Ontario, Canada, N1G 2W1*

Received September 4, 2007; E-mail: vladimir@physics.uoguelph.ca

Abstract: High-resolution solid-state NMR spectroscopy has become a promising tool for protein structure determination. Here, we describe a new dipolar-chemical shift correlation experiment for the measurement of homonuclear $^{13}C-^{13}C$ distances in uniformly $^{13}C,^{15}N$-labeled proteins and demonstrate its suitability for protein structure determination and refinement. The experiments were carried out on the β1 immunoglobulin binding domain of protein G (GB1). Both intraresidue and interresidue distances between carbonyl atoms and atoms in the aliphatic side chains were collected using a three-dimensional chemical shift correlation spectroscopy experiment that uses homogeneously broadened rotational resonance recoupling for carbon mixing. A steady-state approximation for the polarization transfer function was employed in data analysis, and a total of 100 intramolecular distances were determined, all in the range 2.5–5.5 Å. An additional 41 dipolar contacts were detected, but the corresponding distances could not be accurately quantified. Additional distance and torsional restraints were derived from the proton-driven spin diffusion measurements and from the chemical shift analysis, respectively. Using all these restraints, it was possible to refine the structure of GB1 to a root-mean square deviation of 0.8 Å. The approach is of general applicability for peptides and small proteins and can be easily incorporated into a structure determination and refinement protocol.

Introduction

Structural studies of many biological systems, including membrane proteins and amyloid-forming peptides and proteins, remain a challenge for X-ray crystallography and solution NMR, owing to difficulties with crystallization and solubility. Solid-state NMR (SSNMR) is an alternative approach to structure determination in these types of systems.[1–6] Its key advantage is the ability to obtain structural information from a wide range of samples, from protein microcrystals, to amyloid fibrils, to membrane proteins in their native-like lipidic environment. Recent advances in sample preparation techniques[7–9,10–12,13] and

in high field instrumentation and pulse sequence design[14–18] have led to the creation of new efficient methods for chemical shift assignments and structural analysis of the proteins in the solid state. The main source of structural restraints in SSNMR is either $^{13}C-^{13}C$ distances,[5,19,20] collected either using proton-driven spin diffusion (PDSD)[21] or dipolar assisted recoupling (DARR),[22] or interproton distance restraints, obtained through carbon-detected proton–proton spin diffusion.[23–25] Both approaches are capable of establishing the relatively high-

---

† Department of Physics.
‡ Department of Molecular and Cellular Biology.
§ Biophysics Interdepartmental Group.
(1) Opella, S. J. *Nat. Struct. Biol.* **1997**, *4*, 845–848.
(2) Tycko, R. *Curr. Opin. Struc. Biol.* **2004**, *14*, 96–103.
(3) McDermott, A. E. *Curr. Opin. Struc. Biol.* **2004**, *14*, 554–561.
(4) Baldus, M. *Curr. Opin. Struc. Biol.* **2006**, *16*, 618–623.
(5) Castellani, F.; van Rossum, B.; Diehl, A.; Schubert, M.; Rehbein, K.; Oschkinat, H. *Nature* **2002**, *420*, 98–102.
(6) Lange, A.; Giller, K.; Hornig, S.; Martin-Eauclaire, M. F.; Pongs, O.; Becker, S.; Baldus, M. *Nature* **2006**, *440*, 959–962.
(7) Pauli, J.; van Rossum, B.; Forster, H.; de Groot, H. J. M.; Oschkinat, H. *J. Magn. Reson.* **2000**, *143*, 411–416.
(8) Martin, R. W.; Zilm, K. W. *J. Magn. Reson.* **2003**, *165*, 162–174.
(9) Lorch, M.; Fahem, S.; Kaiser, C.; Weber, I.; Mason, A. J.; Bowie, J. U.; Glaubitz, C. *ChemBioChem* **2005**, *6*, 1693–1700.
(10) Li, Y.; Berthold, D. A.; Frericks, H. L.; Gennis, R. B.; Rienstra, C. M. *ChemBioChem* **2007**, *8*, 434–442.
(11) Hiller, M.; Krabben, L.; Vinothkumar, K. R.; Castellani, F.; van Rossum, B. J.; Kuhlbrandt, W.; Oschkinat, H. *ChemBioChem* **2005**, *6*, 1679–1684.
(12) Kloepper, K. D.; Woods, W. S.; Winter, K. A.; George, J. M.; Rienstra, C. M. *Protein Expression Purif.* **2006**, *48*, 112–117.
(13) Frericks, H. L.; Zhou, D. H.; Yap, L. L.; Gennis, R. B.; Rienstra, C. M. *J. Biomol. NMR* **2006**, *36*, 55–71.
(14) Bennett, A. E.; Griffin, R. G.; Vega, S. Recoupling of homo- and heteronuclear dipolar interactions in rotating solids. In *Solid State NMR IV: Methods and Applications of Solid-State NMR*; Blumich, B., Ed.; Springer-Verlag: Berlin, 1994; pp 1–77.
(15) Dusold, S.; Sebald, A. *Annu. Rep. NMR Spectrosc.* **2000**, *41*, 185–264.
(16) Tycko, R. *Annu. Rev. Phys. Chem.* **2001**, *52*, 575–606.
(17) Baldus, M. *Prog. Nucl. Magn. Reson. Spectrosc.* **2002**, *41*, 1–47.
(18) Hughes, C. E.; Baldus, M. *Annu. Rep. NMR Spectrosc.* **2005**, *55*, 121–158.
(19) Castellani, F.; van Rossum, B. J.; Diehl, A.; Rehbein, K.; Oschkinat, H. *Biochemistry* **2003**, *42*, 11476–11483.
(20) Zech, S. G.; Wand, A. J.; McDermott, A. E. *J. Am. Chem. Soc.* **2005**, *127*, 8618–8626.
(21) Szeverenyi, N. M.; Sullivan, M. J.; Maciel, G. E. *J. Magn. Reson.* **1982**, *47*, 462–475.
(22) Takegoshi, K.; Nakamura, S.; Terao, T. *Chem. Phys. Lett* **2001**, *344*, 631–637.

resolution fold of a protein.[5,19,20,26] Various structure refinement methods have also been developed for use in proteins in the solid state. For example, isotropic chemical shift indexing is commonly used for the analysis of a secondary structure,[27−29] while correlating the relative orientations of anisotropic tensors provides information on local and medium-range structures.[30−36,37,38] More recently, the introduction of paramagnetic labels with the purpose of obtaining paramagnetic relaxation enhancements, originally introduced in solution NMR,[39,40] was also applied in solids.[41−43]

One obvious way to establish precise structural constraints in solids is to exploit the fact that molecular motions are generally not sufficiently fast to provide an efficient mechanism for averaging dipolar and chemical shift anisotropy interactions. The anisotropic line broadening associated with the presence of these interactions can be removed through the application of magic angle spinning (MAS),[44,45] whereas the structural information contained in these interactions can be reintroduced through the application of radio frequency (rf) pulses.[14,15] Most notably, heteronuclear rotational echo double resonance (RE-DOR)[46] and frequency-selective homonuclear rotational resonance (R^2)[47,48] have been successfully used to accurately measure distances between specifically placed nuclear spin labels.[49−52] More recently, some of the recoupling methods have

been extended for applications in uniformly ^{13}C,^{15}N labeled solids[53−58] and applied to determine the high-resolution structures of a number of peptides.[59,60]

The main purpose of this paper is to investigate if recoupling techniques can be used to provide accurate structural constraints in uniformly ^{13}C,^{15}N-labeled proteins. We used rotational resonance[47,48] to probe carbonyl side chain distances. In our experiments, the polarization transfer dynamics is monitored as a function of spinning frequency, a so-called rotational resonance width approach.[61] We have recently introduced a homogeneously broadened version of the rotational resonance width experiment, where the broadening of the R^2 matching condition is achieved through the reduction of decoupling power during R^2 mixing.[62] The key advantages of this approach are that (i) the use of reduced decoupling power broadens the R^2 resonance width, so that multiple spin pairs can be recoupled in a single experiment, and (ii) the multispin effects are reduced in the presence of short zero quantum relaxation, enabling a two-spin approximation to be employed for data analysis. A 56 residue protein, $\beta 1$ immunoglobulin binding domain of protein G (GB1) was chosen as a model system for our experiments. It has been extensively studied by various biophysical techniques, including solution and solid-state NMR. Its high-resolution 3D solution[63] and crystal structures,[64] as well as complete ^{13}C and ^{15}N solid-state NMR resonance assignments, are available.[65] We demonstrate that a large number of well-defined $^{13}C-^{13}C$ constraints can in fact be determined from the resonance width curves and that these constraints can be used for structure refinement.

Experimental Section

Sample Preparation. The T2Q mutant of GB1 was heterologously expressed in *E. coli* BL21 (DE3) grown in minimal media (1 g/L ^{15}-NH$_4$Cl and 2 g/L ^{13}C-glucose), induced with 0.5 mM isopropyl β-D-thiogalactoside (IPTG) for 4−5 h. Protein purification was performed as follows: the cell pellet was disrupted by sonication in 20 mM Tris at pH 8.0. The supernatant was subjected to anion exchange (HiTrap Q HP column, Amersham Bioscience, NJ) and size exclusion (HiPrep 16/60 Sephacryl S-100 high-resolution column, Amersham Bioscience, NJ) chromatography. Peak fractions were pooled and dialyzed three times against 2 L of distilled water and finally against 1 L of MilliQ

(23) Wilhelm, M.; Feng, H.; Tracht, U.; Spiess, H. W. *J. Magn. Reson.* **1998**, *134*, 255−260.
(24) Lange, A.; Luca, S.; Baldus, M. *J. Am. Chem. Soc.* **2002**, *124*, 9704−9705.
(25) Tycko, R.; Ishii, Y. *J. Am. Chem. Soc.* **2003**, *125*, 6606−6607.
(26) Lange, A.; Becker, S.; Seidel, K.; Giller, K.; Pongs, O.; Baldus, M. *Angew. Chem., Int. Ed.* **2005**, *44*, 2089−2092.
(27) Wishart, D. S.; Sykes, B. D. *J. Biomol. NMR* **1994**, *4*, 171−180.
(28) Cornilescu, G.; Delaglio, F.; Bax, A. *J. Biomol. NMR* **1999**, *13*, 289−302.
(29) Luca, S.; Filippov, D. V.; van Boom, J. H.; Oschkinat, H.; de Groot, H. J. M.; Baldus, M. *J. Biomol. NMR* **2001**, *20*, 325−331.
(30) Feng, X.; Lee, Y. K.; Sandstrom, D.; Eden, M.; Maisel, H.; Sebald, A.; Levitt, M. H. *Chem. Phys. Lett.* **1996**, *257*, 314−320.
(31) Hong, M.; Gross, J. D.; Griffin, R. G. *J. Phys. Chem. B* **1997**, *101*, 5869−5874.
(32) Feng, X.; Eden, M.; Brinkmann, A.; Luthman, H.; Eriksson, L.; Graslund, A.; Antzutkin, O. N.; Levitt, M. H. *J. Am. Chem. Soc.* **1997**, *119*, 12006−12007.
(33) Costa, P. R.; Gross, J. D.; Hong, M.; Griffin, R. G. *Chem. Phys. Lett.* **1997**, *280*, 95−103.
(34) Hong, M.; Wi, S. Torsion Angle Determination in Biological Solids by Solid-State Nuclear Magnetic Resonance. In *NMR Spectroscopy of Biological Solids*; Ramamoorthy, A., Ed.; Taylor & Francis Group, LLC: Boca Raton, FL, 2006.
(35) Reif, B.; Hohwy, M.; Jaroniec, C. P.; Rienstra, C. M.; Griffin, R. G. *J. Magn. Reson.* **2000**, *145*, 132−141.
(36) Rienstra, C. M.; Hohwy, M.; Mueller, L. J.; Jaroniec, C. P.; Reif, B.; Griffin, R. G. *J. Am. Chem. Soc.* **2002**, *124*, 11908−11922.
(37) Ladizhansky, V.; Jaroniec, C. P.; Diehl, A.; Oschkinat, H.; Griffin, R. G. *J. Am. Chem. Soc.* **2003**, *125*, 6827−6833.
(38) Franks, W. T.; Wylie, B. J.; Stellfox, S. A.; Rienstra, C. M. *J. Am. Chem. Soc.* **2006**, *128*, 3154−3155.
(39) Kosen, P. A. *Methods Enzymol.* **1989**, *177*, 86−121.
(40) Battiste, J. L.; Wagner, G. *Biochemistry* **2000**, *39*, 5355−5365.
(41) Jovanovic, T.; McDermott, A. E. *J. Am. Chem. Soc.* **2005**, *127*, 13816−13821.
(42) Pintacuda, G.; Giraud, N.; Pierattelli, R.; Bockmann, A.; Bertini, I.; Emsley, L. *Angew. Chem., Int. Ed.* **2007**, *46*, 1079−1082.
(43) Nadaud, P. S.; Helmus, J. J.; Hofer, N.; Jaroniec, C. P. *J. Am. Chem. Soc.* **2007**, *129*, 7502−7503.
(44) Andrew, E. R.; Bradbury, A.; Eades, R. G. *Nature* **1958**, *182*, 1659.
(45) Lowe, I. J. *Phys. Rev. Lett.* **1959**, *2*, 285.
(46) Gullion, T.; Schaefer, J. *J. Magn. Reson.* **1989**, *81*, 196−200.
(47) Raleigh, D. P.; Levitt, M. H.; Griffin, R. G. *Chem. Phys. Lett.* **1988**, *146*, 71−76.
(48) Colombo, M. G.; Meier, B. H.; Ernst, R. R. *Chem. Phys. Lett.* **1988**, *146*, 189−196.
(49) McDowell, L. M.; Lee, M. S.; McKay, R. A.; Anderson, K. S.; Schaefer, J. *Biochemistry* **1996**, *35*, 3328−3334.
(50) Mcdermott, A. E.; Creuzet, F.; Griffin, R. G.; Zawadzke, L. E.; Ye, Q. Z.; Walsh, C. T. *Biochemistry* **1990**, *29*, 5767−5775.
(51) Creuzet, F.; Mcdermott, A.; Gebhard, R.; Vanderhoef, K.; Spijkerassink, M. B.; Herzfeld, J.; Lugtenburg, J.; Levitt, M. H.; Griffin, R. G. *Science* **1991**, *251*, 783−786.

(52) Lansbury, P. T.; Costa, P. R.; Griffiths, J. M.; Simon, E. J.; Auger, M.; Halverson, K. J.; Kocisko, D. A.; Hendsch, Z. S.; Ashburn, T. T.; Spencer, R. G. S.; Tidor, B.; Griffin, R. G. *Nat. Struct. Biol.* **1995**, *2*, 990−998.
(53) Jaroniec, C. P.; Tounge, B. A.; Herzfeld, J.; Griffin, R. G. *J. Am. Chem. Soc.* **2001**, *123*, 3507−3519.
(54) Jaroniec, C. P.; Filip, C.; Griffin, R. G. *J. Am. Chem. Soc.* **2002**, *124*, 10728−10742.
(55) Verhoeven, A.; Williamson, P. T. F.; Zimmermann, H.; Ernst, M.; Meier, B. H. *J. Magn. Reson.* **2004**, *168*, 314−326.
(56) Williamson, P. T. F.; Verhoeven, A.; Ernst, M.; Meier, B. H. *J. Am. Chem. Soc.* **2003**, *125*, 2718−2722.
(57) Ramachandran, R.; Ladizhansky, V.; Bajaj, V. S.; Griffin, R. G. *J. Am. Chem. Soc.* **2003**, *125*, 15623−15629.
(58) Ladizhansky, V.; Griffin, R. G. *J. Am. Chem. Soc.* **2004**, *126*, 948−958.
(59) Rienstra, C. M.; Tucker-Kellogg, L.; Jaroniec, C. P.; Hohwy, M.; Reif, B.; McMahon, M. T.; Tidor, B.; Lozano-Perez, T.; Griffin, R. G. *Proc. Natl. Acad. Sci. U.S.A.* **2002**, *99*, 10260−10265.
(60) Jaroniec, C. P.; MacPhee, C. E.; Bajaj, V. S.; McMahon, M. T.; Dobson, C. M.; Griffin, R. G. *Proc. Natl. Acad. Sci. U.S.A.* **2004**, *101*, 711−716.
(61) Costa, P. R.; Sun, B. Q.; Griffin, R. G. *J. Magn. Reson.* **2003**, *164*, 92−103.
(62) Janik, R.; Peng, X.; Ladizhansky, V. *J. Magn. Reson.* **2007**, *188*, 129−140.
(63) Gronenborn, A. M.; Filpula, D. R.; Essig, N. Z.; Achari, A.; Whitlow, M.; Wingfield, P. T.; Clore, G. M. *Science* **1991**, *253*, 657−661.
(64) Gallagher, T.; Alexander, P.; Bryan, P.; Gilliland, G. L. *Biochemistry* **1994**, *33*, 4721−4729.
(65) Franks, W. T.; Zhou, D. H.; Wylie, B. J.; Money, B. G.; Graesser, D. T.; Frericks, H. L.; Sahota, G.; Rienstra, C. M. *J. Am. Chem. Soc.* **2005**, *127*, 12291−12305.
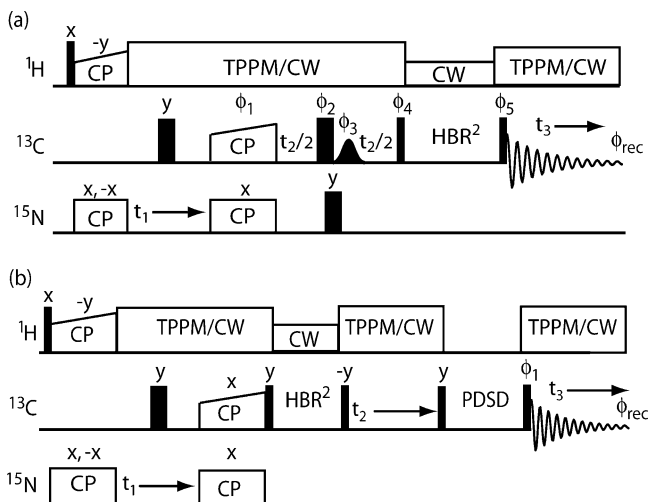
Figure 1. Experimental pulse sequences. The thin and thick dark bars represent $\pi/2$ and π pulses, respectively. In (a), a three-dimensional chemical shift correlation experiment used for HBR^{2}W distance measurements is shown. A selective rotor-synchronized Gaussian π pulse is applied to the carbonyl region. The following phase cycling was used: ϕ_1, ϕ_2, ϕ_3 = (x, x, y, y, −x, −x, −y, −y), ϕ_4 = (y, y, −x, −x, −y, −y, x, x), ϕ_5 = (−y, −y, x, x, y, y, −x, −x), ϕ_{rec} = (x, −x, y, −y, −x, x, −y, y). In (b), a three-dimensional chemical shift correlation experiment for cross-peak assignments is shown. The phase cycling was as follows: ϕ_1 = (x, x, y, y, −x, −x, −y, −y), $\phi_{receiver}$ = (x, −x, y, −y, −x, x, −y, y).

water. Pure protein was concentrated with Centriplus 3 kDa MWCO filters and stored at −20 °C before use. Precipitation of GB1 for NMR studies was performed using a previously published protocol, without modifications.[65] Approximately 15 mg of GB1 precipitate were packed into a 3.2 mm NMR rotor. The sample was centered in the rotor between two cylindrical Vespel inserts. The HBR^{2}W distance measurements and cross-peak assignment experiments were performed on a single U-^{13}C,^{15}N labeled sample. For the identification of intermolecular contacts, some of the experiments were repeated with a uniformly ^{13}C,^{15}N labeled sample mixed in a 1:1 molar ratio with nonlabeled protein. Approximately 15 mg of the diluted protein sample were packed into the rotor.

NMR Experiments. All MAS NMR experiments were performed on a Bruker Avance II spectrometer, operating at 600.130 MHz proton frequency, using a Bruker triple resonance ^{1}H–^{13}C–^{15}N 3.2 mm BioSolids magic angle spinning probe (Bruker USA, Billerica, MA). Two pulse sequences employed in this work are presented in Figure 1. Both start with ^{1}H/^{15}N cross polarization of 2 ms duration, implemented with a radio frequency (rf) field ramped around 55 kHz on the proton channel and with a constant rf field of ∼43−45 kHz on the nitrogen channel. ^{15}N/^{13}C′ cross polarization was performed with an rf carbon field ramped around 42−43 kHz (5% ramp), with a constant rf field of ∼31 kHz on the nitrogen channel and with a CW decoupling proton field of 100 kHz. The ^{15}N/^{13}C′ CP mixing time was 6 ms in all experiments. A proton field of 65 kHz (optimized experimentally) was applied for the two-pulse phase modulation decoupling (TPPM) (7.6 μs TPPM pulse, 15° overall phase shift) during nitrogen t_1 and carbon t_2 indirect chemical shift evolutions. Higher TPPM decoupling of 71 kHz (7μs TPPM pulse, 12° phase shift) was applied during direct ^{13}C acquisition. The $\pi/2$ pulse widths were 2.7 μs, 5 μs, and 6 μs on the ^{1}H, ^{13}C, and ^{15}N channels, respectively. The selective rotor-synchronized Gaussian π pulse applied to carbonyl carbons was around 160−180 μs in length, depending on the spinning frequency. The temperature of the cooling gas was kept at 260 K during the course of all experiments.

Homogeneously Broadened Rotational Resonance Width Experiments. A pulse sequence for distance measurements is shown in Figure 1a. In this experiment, the ^{1}H/^{15}N cross polarization creates transverse ^{15}N coherences, which are subsequently frequency-labeled during t_1

isotropic chemical shift evolution. The ^{13}C π pulse in the middle of the t_1 evolution refocuses one-bond ^{15}N–^{13}C J-couplings. Following t_1 evolution, a band-selective version of ^{15}N/^{13}C′ SPECIFIC CP[66] creates ^{13}C′ single quantum coherences, which are frequency labeled during t_2 isotropic chemical shift evolution. Here, a combination of a hard π pulse and of a soft ^{13}C′-selective Gaussian π pulse refocuses the one-bond homonuclear ^{13}C′−^{13}Cα J-couplings,[67] whereas the hard π pulse on the ^{15}N channel removes the residual line broadening associated with ^{15}N−^{13}C′ J-interactions.

Structurally constraining carbonyl side chain dipolar interactions are recoupled during ^{13}C−^{13}C mixing, following the t_2 period. We used a homogeneously broadened version of R^2 (HBR^2). The broadening is accomplished through the reduction of the decoupling power during R^2 mixing.[62] The experiments were conducted as a function of spinning frequency, which constitutes the fourth pseudo-dimension of the experiment. It was shown previously that such a homogeneously broadened rotational resonance width (HBR^{2}W) implementation has certain advantages over a conventional time-dependent magnetization exchange experiment: (i) the data interpretation does not require prior knowledge or assumptions about zero-quantum relaxation times,[57,61,62] reducing systematic errors associated with this uncertainty, and (ii) many spin pairs can be recoupled in a single experiment, while recoupling of strong one-bond ^{13}C′−^{13}Cα interactions can still be avoided.[62] A constant HBR^2 mixing time of 40 ms was used in all experiments. The CW proton decoupling power during mixing was optimized experimentally to be 47 kHz, the lowest value at which no recoupling of one bond ^{13}C′−^{13}Cα dipolar interactions was observed. Fifteen 3D spectra were recorded at spinning frequencies of 11.3, 11.4, 11.5, 11.6, 11.65, 11.7, 11.75, 11.8, 11.85, 11.9, 11.975, 12.05, 12.15, 12.25, 12.35 kHz. At a proton field of 600 MHz, these spinning frequencies recouple carbonyls and aliphatic side chain carbons through the $n = 2$ R^2 matching condition.

The schematic representation of the evolution of the relevant part of the density matrix, starting with the nitrogen magnetization following ^{1}H/^{15}N CP, can be written as follows:

$$N_{ix} \xrightarrow{t_1} N_{ix}\cos\Omega_{N_i}t_1 \xrightarrow{DCP} C'_{i-1x}\cos\Omega_{N_i}t_1 \xrightarrow{t_2} C'_{i-1x}\cos\Omega_{N_i}t_1\cos\Omega_{C'_{i-1}}t_2 \xrightarrow{HBR^2} \quad (1)$$

$$\rightarrow (1-\alpha)C'_{i-1x}\cos\Omega_{N_i}t_1\cos\Omega_{C'_{i-1}}t_2 + \alpha C_{jx}^X\cos\Omega_{N_i}t_1\cos\Omega_{C'_{i-1}}t_2$$

$$\xrightarrow{t_3} \underline{(1-\alpha)C'_{i-1x}\cos\Omega_{N_i}t_1\cos\Omega_{C'_{i-1}}t_2 e^{i\Omega_{C'_{i-1}}t_3}} + \underline{\underline{\alpha C_{jx}^X\cos\Omega_{N_i}t_1\cos\Omega_{C'_{i-1}}t_2 e^{i\Omega_{C_j^X}t_3}}}$$

In the expression above, N_{ix}, C'_{i-1x}, and C_{jx}^X denote spin operators corresponding to single quantum coherences of nitrogen, carbonyl, and aliphatic side chain ($X = \gamma$, δ, etc.) spins, and Ω_{N_i}, $\Omega_{C'_{i-1}}$, and $\Omega_{C_j^X}$ are their respective isotropic chemical shifts. This pathway is collected according to a TPPI phase sensitive scheme in t_1 and t_2 dimensions.

There are generally two sets of peaks observed in the Fourier transformed 3D spectra. The pseudo-diagonal peaks of relative intensity $(1-\alpha)$ result from the singly underlined component of the density matrix in eq 1 and have $\Omega_N/\Omega_{C'_{i-1}}/\Omega_{C'_{i-1}}$ shifts in the F$_1$/F$_2$/F$_3$ dimensions, respectively. These peaks determine the origin of the R^2 magnetization transfer. The cross-peaks of relative intensity α, doubly underlined in eq 1, occur at shifts of $\Omega_N/\Omega_{C'_{i-1}}/\Omega_{C_j^X}$ and correspond to the aliphatic carbons ^{13}C^X[j], through-space coupled to ^{13}C′[i−1]. The relative intensities of these peaks, α, depend on the strengths of the dipolar interaction between ^{13}C′[i−1] and ^{13}C^X[j] spins, on the spinning frequency, and on the residual coupling to the proton bath.

Cross-Peak Assignment Experiments. Within each interacting pair of spins ^{13}C′[i−1]−^{13}C^X[j], the carbonyl spin can be identified in the 3D correlation spectra according to the known ^{15}N[i]−^{13}C′[i−1] correlation pattern.[65] In contrast, the assignments of the aliphatic cross-

(66) Baldus, M.; Petkova, A. T.; Herzfeld, J.; Griffin, R. G. *Mol. Phys.* **1998**, *95*, 1197−1207.
(67) Straus, S. K.; Bremi, T.; Ernst, R. R. *Chem. Phys. Lett.* **1996**, *262*, 709−715.

peaks are generally ambiguous, because they are only based on the chemical shifts of the $^{13}C^X[j]$ spins. The cross-peak assignments were assisted with a series of three-dimensional chemical shift correlation experiments shown in Figure 1b. The polarization transfer pathway here is the same as the one explained in eq 1 for the HBR^2 experiment, except that the carbonyl chemical shift evolution is replaced by the chemical shift evolution of the aliphatic spins and by an additional $^{13}C-^{13}C$ mixing step. The resulting $^{15}N[i]-^{13}C^X[j]-^{13}C^Y[j]$ ($X = \gamma, \delta$; $Y = \alpha, \beta$, etc.) correlation shares $^{15}N[i]$ and $^{13}C^X[j]$ shifts with the HBR^2 $^{15}N[i]-^{13}C'[i-1]-^{13}C^X[j]$ correlation and also allows identification of $^{13}C^X[j]$ spins according to the unique intraresidue $^{13}C^X[j]-^{13}C^Y[j]$ correlation pattern. A total of four experiments for cross-peak assignments were recorded at spinning frequencies of 11.5, 11.65, 11.9, and 12.05 kHz. The assignment strategies are further discussed in the Results and Discussion section.

For the identification of intermolecular contacts, three additional HBR^2 experiments were recorded at spinning frequencies of 11.3, 11.65, and 12.25 kHz in a diluted sample. Spectra at 11.3 and 11.65 kHz were recorded with 16 scans, and the experiment at 12.25 kHz was recorded with 8 scans.

Proton-Driven Spin Diffusion Experiments. To get additional constraints for structure calculation and refinement, HBR^{2}W measurements were supplemented with a set of distance restraints derived from 2D and 3D spin diffusion spectra. A 3D NCOCX spectrum was recorded using the pulse sequence of Figure 1a, except that no decoupling was applied during COCX mixing. The 3D NCACX spin diffusion experiment was recorded using a previously published pulse sequence.[19] In addition, a 2D $^{13}C-^{13}C$ spin diffusion correlation spectrum was taken. All spin diffusion experiments were recorded with a 500 ms mixing time. The $^{13}C-^{13}C$ distance restraints derived from these spin diffusion spectra were used for structure calculation as discussed in the following section.

Data Analysis. Experimental data were processed with NMRPipe.[68] Processing parameters are provided in the respective figure captions. Chemical shift was indirectly referenced to DSS using the chemical shift of the downfield ^{13}C resonance in adamantane (40.48 ppm).[69] The general positions of the cross-peaks in our spectra were found to be very similar to the published data, with most peaks found to be within 0.2 ppm from previously published chemical shifts,[65] although some ^{15}N shifts were found to deviate by as much as 0.5 ppm. For reference purposes, the assignment table derived from a series of 2D ($^{13}C-^{13}C$, NCA, NCO) and 3D (NCACX, NCOCX) correlation experiments and used in the analysis of the HBR^2 experiments is given in the Supporting Information. Processed data were analyzed using Sparky software, version 3.1 (T. D. Goddard and D. G. Kneller, University of California, San Francisco, CA). Peak volumes were extracted with automated fitting to three-dimensional Gaussians.

The HBR^{2}W curves (i.e., cross-peak intensities as functions of spinning frequencies) were fitted using a steady-state approximate solution for a two-spin system under short zero-quantum relaxation conditions:[62]

$$S(\Delta) = \left\langle \frac{1}{2}\left(1 - \exp\left\{-\frac{4|\omega_D^{(2)}|^2 R_{ZQ}}{\Delta^2 + R_{ZQ}^2}t_{mix}\right\}\right)\right\rangle_{powder} \quad (2)$$

Here t_{mix} and R_{ZQ} are the HBR^2 constant mixing time (40 ms) and zero quantum relaxation rate, $R_{ZQ} = 1/T_2^{ZQ}$, respectively, $\Delta = \delta_I - \delta_S - 2\nu_R$ depends on the spinning frequency ν_R and measures the deviation from the exact $n = 2$ rotational resonance condition. δ_I, δ_S are the chemical shifts of spins I (carbonyl) and S (aliphatic spin), respectively. The effective dipolar interaction $\omega_D^{(2)}$ was calculated as[70]

(68) Delaglio, F.; Grzesiek, S.; Vuister, G. W.; Zhu, G.; Pfeifer, J.; Bax, A. *J. Biomol. NMR* **1995**, *6*, 277–293.
(69) Morcombe, C. R.; Zilm, K. W. *J. Magn. Reson.* **2003**, *162*, 479–486.
(70) Levitt, M. H.; Raleigh, D. P.; Creuzet, F.; Griffin, R. G. *J. Chem. Phys.* **1990**, *92*, 6347–6364.

$$\omega_D^{(2)} = b_{IS}\frac{1}{4}\sin^2\beta \quad (3)$$

where $b_{IS} = (-\mu_0/4\pi)(\gamma^2\hbar/r^3)$ is the dipolar coupling constant for a homonuclear spin pair, r is the internuclear distance, and β is the Euler angle defining the orientation of the internuclear vector with respect to the rotor-fixed frame. The effects of chemical shift anisotropy (CSA) were neglected in the fitting but were taken into account through the introduction of the systematic error as explained in the Results and Discussion section.

We have shown previously that the steady-state approximation accurately describes R^2 polarization transfer in situations when the zero quantum relaxation rate is large compared to the effective interaction strength.[62] This assumption holds well under low decoupling conditions used in this work.

Equation 2 assumes that the aliphatic cross-peaks are normalized per initial intensity of the corresponding carbonyl peak. To avoid the additional time-consuming procedure of collecting reference spectra at zero mixing time, the aliphatic cross-peak intensities were normalized with respect to the sum of all peaks occurring at $\Omega_{N_i}/\Omega_{C'_{i-1}}$ shifts in the F_1 and F_2 indirect dimensions, including spinning sidebands:

$$S_{N_iC'_{i-1}C_j^X}^{norm} = \frac{S_{N_iC'_{i-1}C_j^X}}{\sum_k S_{N_iC'_{i-1}C_k}} \quad (4)$$

Here, $S_{N_iC'_{i-1}C_j}^X$ is the volume intensity of the cross-peak of interest, $S_{N_iC'_{i-1}C_k}$ is the intensity of the peak occurring at shifts $\Omega_{N_i}/\Omega_{C'_{i-1}}/\Omega_{C_k}$, and the summation is extended over all cross-peaks at $\Omega_{N_i}/\Omega_{C'_{i-1}}/\Omega_{C_k}$ shifts along F_3. This normalization procedure assumes that the longitudinal T_1 relaxation times of carbon spins are long on the time scale of HBR^2 mixing of 40 ms, and thus the total polarization is conserved during R^2.

Statistical analysis of random errors was performed using in-house Monte Carlo simulations, implemented in FORTRAN 77. Briefly, the analytical expression 2 was used to generate a two-dimensional grid of R^{2}W curves simulated as a function of relaxation rate R_{ZQ} and an internuclear distance for each spin pair, using experimental mismatch values Δ. A typical size of the grid was 2500 curves, for distances in the range 2.5–7.5 Å incremented in a step of 0.1 Å and for relaxation times from 0.1 to 5 ms incremented in a step of 0.1 ms. Such a grid can be generated in less than 1 min, benefiting from the use of the analytical solution of eq 2 for the signal intensity. Once the analytical solution grid was generated, the best fit to the experimental R^{2}W curve was found, and the root-mean-square deviation (rmsd) was computed. The rmsd was used to generate random noise according to a Gaussian distribution with zero mean and a standard deviation equal to the rmsd. The simulated noise was added to each point of the best fit, and the resulting curves were refit using the same solution grid. This procedure was repeated 10 000 times. A histogram showing the frequencies of occurrence of each distance in this procedure was used to extract a range of internuclear distances at a 95% confidence level.

Results and Discussion

$^{15}N[i]-^{13}CO[i-1]$ Spectral Resolution in GB1. The indirect F_1-F_2 projection of the $^{15}N-^{13}CO$ spectrum recorded at a spinning frequency of 11.65 kHz is shown in Figure 2. The cross-peaks in the spectrum identify the origin of the polarization transfer process, and the resolution provides the basis for the site-specific analysis of the 3D spectra. Generally, the resolution in the indirect carbonyl chemical shift dimension observed in this work is higher than the one observed directly, owing to the homonuclear $J_{COC\alpha}$ decoupling implemented in the pulse sequence.
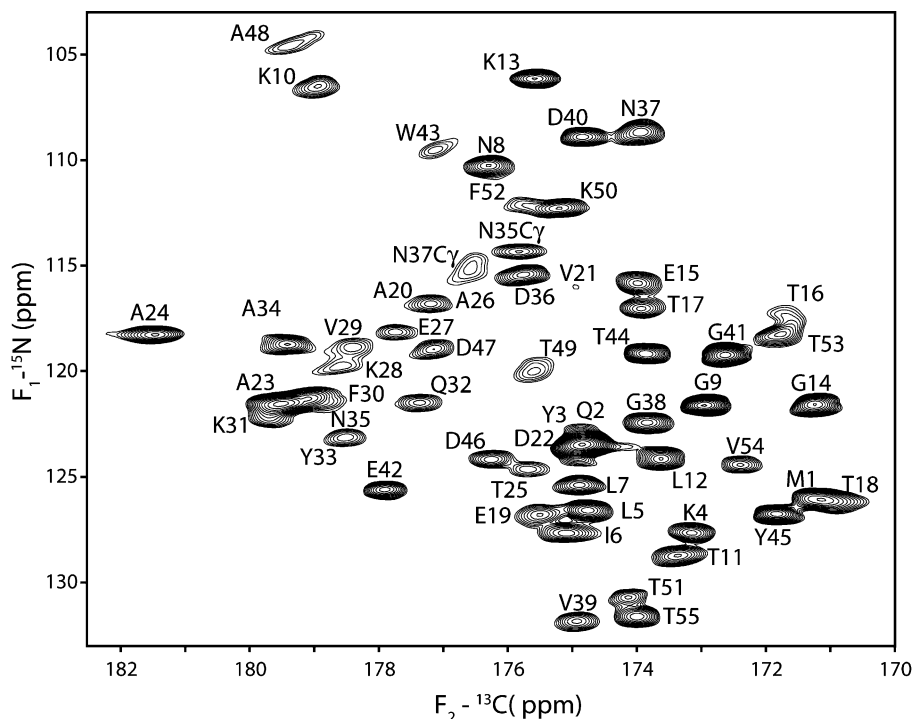
Figure 2. 2D $^{15}N[i]$–$^{13}C'[i-1]$ indirect F_1–F_2 projection of the 3D HBR^2 spectrum, recorded at a spinning rate of 11.65 kHz. 84 real data points with 200 μs dwell time were taken in t_1, and 52 real data points with 125 μs dwell time were taken in t_2. The spectrum was recorded with 12 scans and with a recycling delay of 2.3 s. Forward prediction of 35 points and 52 points was applied to the raw data in the t_1 and t_2 dimensions, respectively. Data were processed with exponential line broadening of 5.0 Hz in the t_1 dimension, Lorentzian-to-Gaussian apodization (5.0 Hz of Gaussian line broadening and 10 Hz of Lorentzian line narrowing) in the t_2 indirect dimension, and with the $\pi/2.5$-shifted squared sinusoidal function in the t_3 direct ^{13}C dimension. All peaks are labeled according to their carbonyl/carboxylate shifts.

The typical experimentally observed line widths were ∼0.4– 0.5 ppm for the ^{13}C indirect dimension and ∼0.5–0.6 ppm for the ^{15}N dimension, as estimated from the 2D ^{15}N–^{13}CO projection spectra.

Of the expected 55 backbone $^{15}N[i]$–$^{13}CO[i-1]$ peaks, a total of 45 are well resolved, and their corresponding volume intensities can be reliably extracted from the 3D spectra. The remaining 10 backbone cross-peaks show some degree of spectral overlap. In particular, the Q2N-M1C′ and T19N-T18C′ peaks at about 126/171.2 ppm overlap completely, and their contributions to the formation of the aliphatic cross-peaks cannot be disentangled. There is a similar situation for the heavily overlapping group of Y3N-Q2C′, K4N-Y3C′, A23N-D22C′ peaks at around 123.6/174.8 ppm and for the V21N-A20C′ and E27N-A26C′ peaks at about 116.8/177.3 ppm. Partially overlapping peaks T51N-K50C′ and T53N-F52C′ at around 112.2/155.6 ppm could not be integrated accurately, but their peak volumes could be estimated from the 3D spectra. The D22N-V21C′ at 116/175 ppm cross-peak is very weak, probably because of the high mobility of V21.[65]

In addition to $^{15}N[i]$–$^{13}CO[i-1]$ backbone correlations, two side chain cross-peaks corresponding to the nitrogen–carboxylate correlations in asparagines are observed. A total of five side chain ^{15}N–^{13}C correlations of this type are expected, but only two, $^{15}N\delta$-$^{13}C\gamma$ of N35 and N37 at 114.3/175.8 ppm, and 115.1/176.6 ppm, respectively, can be clearly seen in the 2D indirect projection of Figure 2. Both of these residues are located inside the α-helical secondary structure, and their side chains are relatively immobile. In contrast, the side chain correlations in Q32, Q2, and N8 are of much lower intensity in the full 3D

spectrum, probably due to their increased mobility. These peaks are missing in this 2D projection.

HBR^2 Spectra. At 600 MHz, most carbonyl-aliphatic side chain spin pairs have their $n = 2$ R^2 conditions in the range of 11.3–12.35 kHz. Matching this condition within the HBR^2 recoupling bandwidth results in the formation of the cross-peaks. Figure 3 shows representative 2D planes (F_1–F_3, ^{15}N indirect and ^{13}C direct dimensions) of the full 3D HBR^2 experiments measured at different spinning rates. The left panel shows a 2D plane of the $^{15}N[i]$–$^{13}CO[i-1]$–$^{13}CO[i-1]$ part of the spectrum taken at 11.65 kHz spinning frequency, while three panels on the right show aliphatic peaks detected at 11.5 kHz, 11.6 kHz, and 11.65 kHz, respectively. Cross-peaks aligned horizontally represent interacting spin pairs. For example, there is a strong interaction between N37C′ and V39γ1 carbons, whereas V39γ1 also interacts strongly with G38C′. Most of the peaks observed in the spectra in Figure 3 correspond to either intraresidue (e.g., T17C′-T17Cγ2 or T44C′-T44Cγ2, with exact $n = 2$ R^2 conditions at 11.483 kHz, and 11.536 kHz, respectively) or sequential (e.g., E15C′-T16Cγ2, G38C′-V39γ1 with exact $n = 2$ R^2 conditions at 11.618 kHz and 11.468 kHz, respectively) connectivities. These contacts mostly constrain local side chain conformations. There are also some medium and long range interactions (e.g., N37C′-V39γ1 and E15C′-T44Cγ2, with exact matching conditions at 11.476 kHz and 11.544 kHz, respectively), which report on the secondary structure and global fold of the protein. In the latter case, the E15C′-T44Cγ2 cross-peak corresponds to an intermolecular interaction, as discussed in the following section.
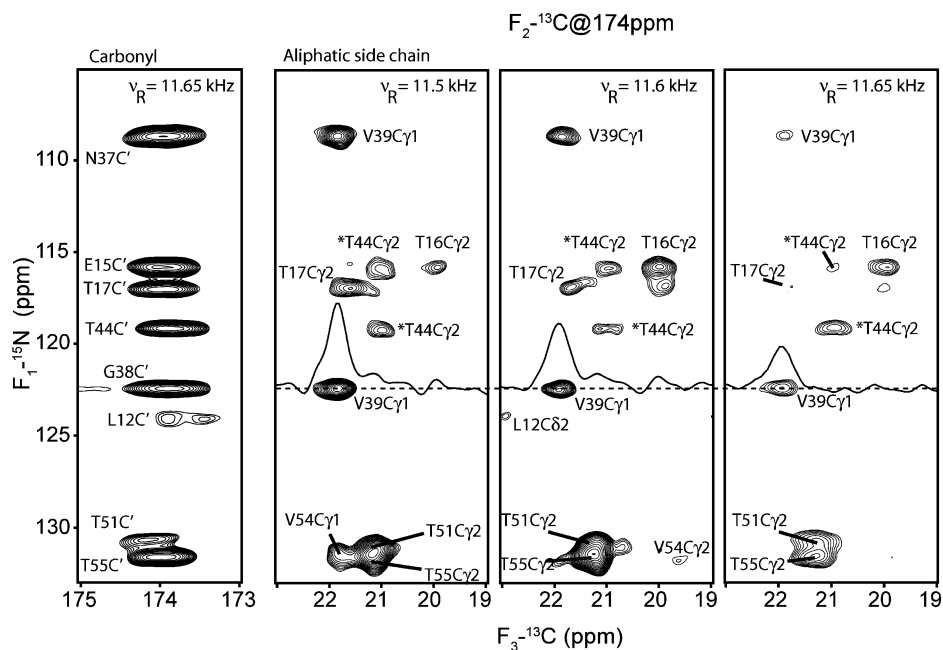
Figure 3. 2D planes (F_1–F_3) of the 3D HBR^2 experiments. The acquisition and processing parameters are identical to those given in the caption to Figure 2. All F_1–F_3 2D planes were taken at an F_2 shift of 174 ppm. The left panel shows the carbonyl region at a spinning rate of 11.65 kHz, and the other three panels show the aliphatic side chain carbon regions at spinning rates of 11.5, 11.6, and 11.65 kHz, respectively. Contours are cut at the same levels in all three figures. The peaks that align horizontally are the interacting carbonyl-side chain carbon pairs. Cross-peaks marked by asterisks are used as examples of assignments in the text and in Figure 5.

Distance Estimation. The rotational resonance polarization transfer depends on the internuclear distance and on the residual coupling to the proton bath, characterized by a zero quantum relaxation parameter. In the R^{2}W experiment, both parameters can be extracted unambiguously.[61] The use of low decoupling power further facilitates the increase of the homogeneous line width of the zero quantum transition.[62] As a result, the R^2 recoupling can be observed over a wide range of spinning frequencies, as evident from the 2D spectra of Figure 3. The transfer efficiencies are the highest at or close to the exact R^2 matching conditions and reach 46% for intraresidue ^{13}C′–^{13}Cγ two-bond transfers in alanines, e.g., in A48C′-Cβ. On the other hand, the efficiencies can be as low as a few percent for long-range transfers, e.g., in N8C′-V54Cγ2 (6.04 Å in the X-ray structure[38]). In the latter case, however, the cross-peaks can typically be observed only when the spinning frequencies are very close to the exact $n = 2$ R^2 condition, and the distances cannot be extracted reliably from the NMR data. Accordingly, all cross-peaks have been classified in two groups. All peaks that could be observed at more than three spinning frequencies were considered to be statistically significant. An additional two points of intensity equal to experimentally measured noise values were added on both sides of these HBR^{2}W curves. These peaks were fitted as explained in the Data Analysis section. Two typical HBR^{2}W curves for the E42C′-V54Cγ1 and E15C′-T16Cγ2 spin pairs are shown in Figure 4, together with their best fits and the results of Monte Carlo analysis.

Peaks with nonzero intensities at three or less spinning frequencies belong to the second group. These, typically low-intensity peaks, were used only for distance estimation, with corresponding distances defined to be in the range 2.9–7.5 Å.

A number of factors must be taken into account in the analysis of the R^{2}W data. First, the second-order spinning side bands of carbonyls occur in the aliphatic region of the 3D HBR^2 carbon

spectrum and can obscure cross-peaks of interest. This in turn may result in an overestimation of dipolar coupling constants. The overlap can only occur in the close vicinity of the $n = 2$ R^2 condition and for a single value of spinning frequency (the spinning frequency was incremented in 50–100 Hz, resulting in the increment of the second sideband position by 100–200 Hz, which exceeds the aliphatic line widths). The relative intensities of the second-order sidebands were estimated from experimental spectra and were found to be on the order of 1–4% of the main carbonyl peaks. Such a small contribution does not significantly disturb the intensities of strong cross-peaks but can make a significant contribution to the intensities of weak cross-peaks. In cases where this overlap does happen, the perturbed points were simply removed from the data and were not used for fitting.

The correct integration of the carbonyl cross-peaks could also be affected by an overlap between one-bond interresidue ^{15}N-[i]–^{13}C′[i-1] and two-bond intraresidue ^{15}N[j]–^{13}C′[j] cross-peaks. We use different indices "*i*" and "*j*" here to emphasize that the overlapping peaks may be completely unrelated to one another. To estimate the relative efficiency of the two-bond transfers, we identified 29 well-resolved two-bond ^{15}N[j]–^{13}C′[j] cross-peaks in the carbonyl part of the 3D spectra. Their volume integrals were found to vary from 1% to 10% of the ^{15}N[i]–^{13}C′[i-1] peaks. Thus, if any overlap happens between these two groups of peaks, the aliphatic normalized cross-peak intensities may be underestimated by 10% at most, and this may result in an error of ~0.1–0.2 Å in distance. These errors are much smaller than other systematic errors discussed below, and therefore, were not considered in our data analysis.

Cross-Peak Assignments. From all aliphatic resonances in GB1, nine have unique chemical shifts (M1Cϵ (15.8 ppm), I6Cδ1 (12.7 ppm), L12Cδ2 (23.0 ppm), T11Cγ2 (22.6 ppm), T18Cγ2 (18.8 ppm), A20Cβ (23.8 ppm), V29Cγ1 (22.3 ppm),
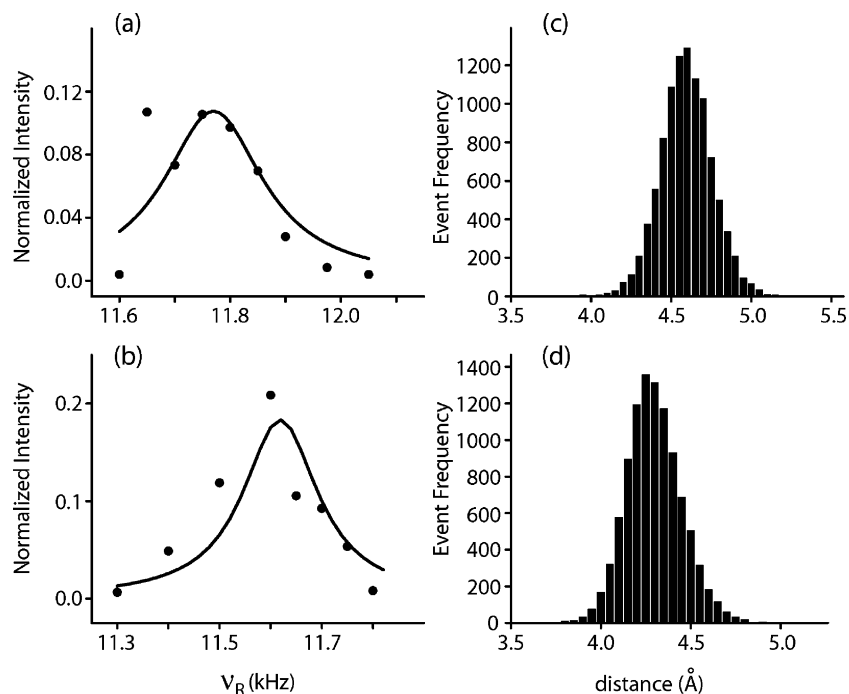
Figure 4. Distance fitting and estimation of random errors by Monte Carlo simulation. Experimentally measured normalized intensities for a long-range E42C'-V54Cγ1 interaction in (a), and for an intermolecular E15C'-T16Cγ2 dipolar interaction in (b), are shown in solid circles. Solid lines represent the best fits to the experimental data, obtained using the simplified two-spin model of eq 2 The best fit curves were generated using $r = 4.6$ Å, $T_2^{ZQ} = 0.8$ ms for E42C'-V54Cγ1 in (a) and $r = 4.3$ Å, $T_2^{ZQ} = 1.07$ ms for E15C'-T16Cγ2 in (b). (c) Ten thousand iterations of Monte Carlo fitting for E42C'-V54Cγ1, resulting in a 95% confidence interval of 4.3−4.9 Å for the internuclear distance. (d) Ten thousand iterations of Monte Carlo fitting for E15C'-T16Cγ2, resulting in a 95% confidence interval of 4.0−4.6 Å for the internuclear distance.

Table 1. Cross-Peaks with Aliphatic Shifts in the Range 20.5−21.5 ppm Observed in the 3D HBR^2 Experiment at $\nu_R = 11.65$ kHz

cross-peak	^{15}N shift (ppm)	$^{13}C'$ shift (ppm)	$^{13}C\gamma$ shift (ppm)
K50C'-T51Cγ2	112.3	175.3	21.2
E15 C'-T44Cγ2	115.8	174.0	21.03
T44C'-T44Cγ2	119.1	173.9	21.03
T25C'-T25Cγ2	124.6	175.8	21.5
T51C'-T51 Cγ2	130.7	174.2	21.2
T55C'-T55 Cγ2	131.7	174.0	21.3

A48Cβ (19.1 ppm), V54Cγ2 (19.7 ppm)), and their assignments were straightforward. A total of 8 intraresidue, 13 sequential, 6 medium-range, and 8 long-range distances could be unambiguously identified from the chemical shift analysis of 3D HBR^2 spectra alone (Table S2, Supporting Information). These constraints were not sufficient to follow an iterative cross-peak assignment procedure. To assist cross-peak assignments, additional three-dimensional experiments shown in Figure 1b were conducted. As an example, we will describe the assignment of two cross-peaks detected at 115.8/21.0 ppm and 119.2/21.0 ppm (indicated by asterisks) in Figure 3. In addition to these two peaks, four additional strong cross-peaks with aliphatic shifts around 21 ppm can be observed in the full 3D spectrum. A full list of these peaks is given in Table 1.

In principle, these peaks can be assigned to any of a total of six carbon atoms in the protein resonating around 21 ppm: V21Cγ2 (21.1 ppm), V29Cγ2 (21.1 ppm), T44Cγ2 (21.0 ppm), T51Cγ2 (21.3 ppm), T53Cγ2 (21.3 ppm), and T55Cγ2 (21.3 ppm). This relatively high ambiguity in the assignment can be removed spectroscopically, by using the experiment shown in Figure 1b. The $^{15}N[i]$−$^{13}C^X[j]$−$^{13}C^Y[j]$ correlations established in this experiment share $^{15}N[i]$ and $^{13}C^X[j]$ chemical shifts with

the $^{15}N[i]$−$^{13}C'[i-1]$−$^{13}C^X[j]$ correlations obtained in the HBR^2 spectrum. Since all peaks in Table 1 have unique nitrogen shifts, they are readily recognizable in the $^{15}N[i]$−$^{13}C^X[j]$−$^{13}C^Y[j]$ spectra.

A representative 2D plane taken at the F$_2$ shift of 21.15 ppm of the full 3D assignment spectrum is shown in Figure 5. The $^{13}C^X$−$^{13}C^Y$ intraresidue correlations provide unambiguous assignments for many peaks according to the known amino acid correlation patterns. In particular, the cross-peak at a ^{15}N shift of 119.2 ppm marked with asterisks in Figures 3 and 5 can be assigned to T44Cγ2. Likewise, cross-peaks at nitrogen shifts of 112.3, 124.6, 130.7, and 131.7 ppm can be readily assigned to T51Cγ2, T25Cγ2, T51Cγ2, and T55Cγ2, respectively, based on the unique $^{13}C\gamma$−$^{13}C\beta$ and $^{13}C\gamma$−$^{13}C\alpha$ intraresidue correlation patterns.

The intraresidue correlation at 115.3/72.8 ppm appears to be slightly shifted along the nitrogen dimension, compared to the weak pseudo-diagonal peak at 115.8/21.1 ppm in Figure 5, probably owing to its low signal-to-noise ratio. Thus, it can only be tentatively assigned to T44Cβ. Later measurements in the 50% diluted sample confirmed this assignment.

The experiments conducted at four spinning frequencies have provided assignments for an additional 11 intraresidue, 9 sequential, 7 medium-range, and 3 long-range constraints, bringing the total number of constraints to 19 intraresidue, 22 sequential, 13 medium-range, and 11 long-range. These constraints were used for an iterative assignment procedure as discussed previously by Zech et al.[20] Briefly, the assigned constraints were combined with 84 dihedral angles obtained from the chemical shift analysis using TALOS[28] and subjected to a standard structure calculation algorithm performed using
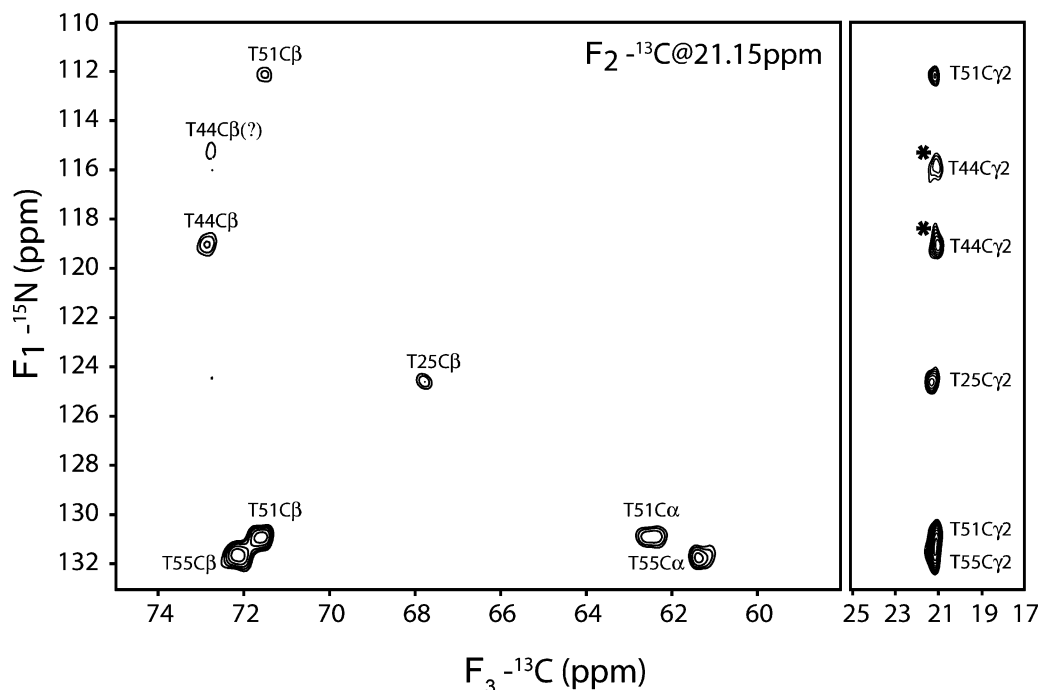
Figure 5. 2D F_1−F_3 plane of the 3D assignment experiment. The spectrum was recorded with 68 real data points and with a dwell time of 200 μs in t_1 (TPPI) and with 500 real data points and with a dwell time of 27.6 μs in t_2 (TPPI). 30 real data points were linearly predicted in t_1. Data were processed with the $\pi/2$-shifted squares sinusoidal window function in all three dimensions. The spinning frequency was 11.5 kHz. The number of scans was 2, and the recycle delay was 2.4 s. The 2D plane shown here is taken through the F_2 frequency of 21.15 ppm. Cross-peaks in the right panel are also observed in the HBR^2 spectrum. Intraresidue correlations to Cα/Cβ carbons established through PDSD mixing of 50 ms appear in the left panel.

Xplor-NIH.[71] The calculated structure was used as a template for removing some of the ambiguities in the assignments, and the newly assigned constraints were used to refine the template structure. A total of four iterations were required to assign all but 33 cross-peaks. Additional information on the convergence of this iterative cross-peak assignment procedure can be found in the Supporting Information.

Identification of Intermolecular Contacts. In compact and highly ordered microcrystals of GB1, it is possible to observe intermolecular contacts. It was demonstrated previously that isotopic dilution of the sample helps to attenuate or suppress the cross-peaks resulting from intermolecular contacts and to distinguish them from intramolecular peaks. To follow this strategy, we prepared a sample precipitated from a mixture containing labeled and natural abundance GB1 in a 1:1 molar ratio. In this diluted sample, the signals resulting from inter-molecular interactions are expected to be significantly attenuated and should be easily identifiable in the HBR^2 spectra. To avoid repeating the whole set of HBR^2 experiments with the diluted sample, the potential intermolecular contacts were first identified based on the analysis of two possible crystal structures,[38,64] as shown in Figure 6.

The HBR^2 experiments were repeated in the diluted sample to probe these specific contacts. An alternative approach that does not require prior knowledge of the X-ray structure was demonstrated previously by Oschkinat and co-workers,[19] and by McDermott and co-workers.[20] Experiments using broad-banded DARR or PDSD ^{13}C−^{13}C mixing appear to be optimal for the identification of the intermolecular interactions in diluted samples, as these contacts can be identified in a single experiment.
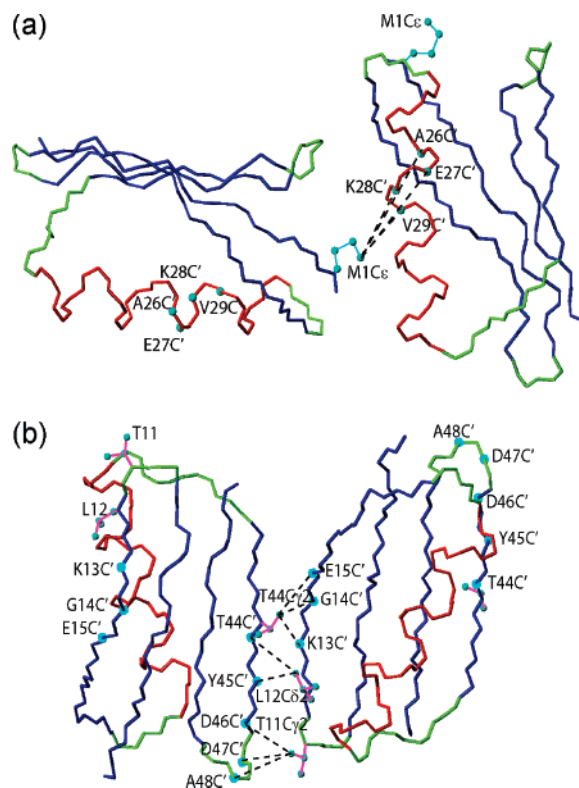
(71) Schwieters, C. D.; Kuszewski, J. J.; Tjandra, N.; Clore, G. M. *J. Magn. Reson.* **2003**, *160*, 65−73.

Figure 6. Intermolecular carbonyl−side chain interaction detected in HBR^2 experiments. Both types of interactions between the N-terminal methionine and α-helix shown in (a) and between β2 and β3 strands shown in (b) are present in crystals with trigonal packing.[64] Only contacts between residues located in β2 and β3 strands of GB1 shown in (b) are present in the orthorhombic packing.[38]

Of the 12 intermolecular interactions detected in our experi-ments, 4 take place between the side chain of methionine and
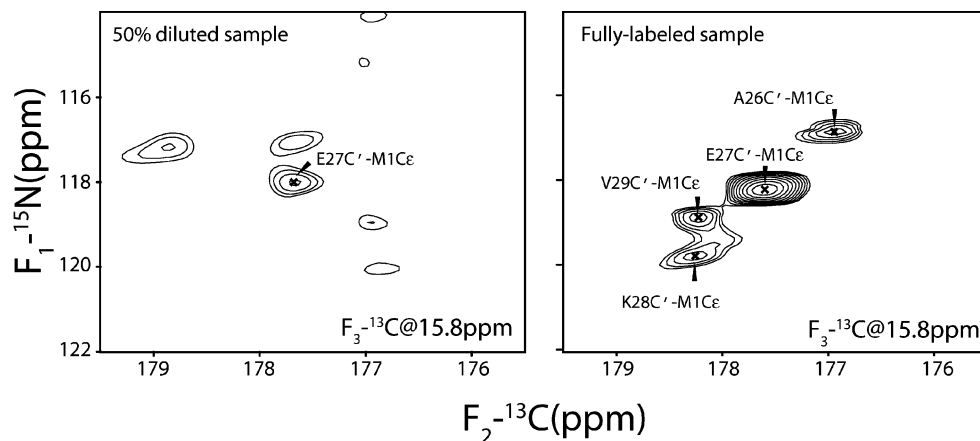
Figure 7. 2D planes of the HBR^2 experiment recorded in 50% diluted and fully labeled samples, at a spinning frequency of 12.25 kHz under identical decoupling conditions. The planes were taken at 15.8 ppm in the F$_3$ direct dimension at the position of M1Cϵ). The processing parameters were identical to those given in the caption to Figure 2. Both spectra are normalized with respect to the intensity of the carbonyl K28N-E27C′ cross-peak. All peaks shown in this figure are significantly attenuated in the diluted sample and were attributed to intermolecular interactions.

Table 2. A List of Intermolecular Contacts Detected in HBR^2 Experiments, Extracted Distances, and Their Comparison with Two Crystal Packing Forms for GB1

intermolecular contacts	distances (Å)		
	orthorhombic (PDB: 2GI9)	trigonal (PDB: 1PGB)	SSNMR
K13C′-T44Cγ2	5.1	5.1	5.2 ± 0.8
G14C′-T44Cγ2	4.5	4.5	2.9 − 7.5
E15C′-T44Cγ2	4.4	4.3	4.5 ± 0.7
T44C′-L12Cγ2	6.1	5.1	2.9 − 7.5
Y45C′-L12Cγ2	5.5	4.1	2.9 − 7.5
D46C′-T11Cγ2	4.7	4.6	2.9 − 7.5
D47C′-T11Cγ2	4.4	4.4	2.9 − 7.5
A48C′-T11Cγ2	5.5	5.5	4.5 ± 0.7
A26C′-M1Cϵ	>10	10.0	2.9 − 7.5
E27C′-M1Cϵ	>10	10.0	4.5 ± 0.7
K28C′-M1Cϵ	>10	7.6	2.9 − 7.5
V29C′-M1Cϵ	>10	5.5	2.9 − 7.5

backbone carbonyls of A26, E27, K28, and V29, all located in the α-helix (Figure 6a). The corresponding cross-peaks are significantly attenuated in the spectra of the diluted sample, as shown in Figure 7. Interestingly, the presence of these peaks is completely inconsistent with the orthorhombic crystal packing.[38]

The data are more consistent with another type of lattice that GB1 molecules can form, trigonal,[64] although the distances derived from our NMR measurements appear to be shorter than those extracted from the X-ray structure (Table 2). This indicates a more compact packing in the nanocrystals, compared with crystals of macroscopic size. An additional eight interactions take place between residues located on the β2- and β3-strands in GB1 (Figure 6b). They are consistent with both orthorhombic and trigonal packing forms.

Systematic Uncertainties in the Measured Distances. Possible sources of systematic errors in R^{2}W measurements have been discussed previously.[62,72] The largest is associated with uncertainty in the relative orientation of the carbonyl chemical shift anisotropy and dipolar tensors. It was shown that the complete omission of the CSA results in the systematic errors of ca. ±0.6 Å, independent of the T$_2^{ZQ}$ relaxation. In most cases, this uncertainty was the dominant source of error.

(72) Ramachandran, R.; Lewandowski, J. R.; van der Wel, P. C. A.; Griffin, R. G. *J. Chem. Phys.* **2006**, *124*, 214107.

Another systematic uncertainty may result from the presence of multispin effects, which is obvious from Figure 3: V39Cγ1 interacts simultaneously with N37C′ and G38C′ forming a three-spin system, whereas the T16Cγ2, E15C′, T44Cγ2, and T44C′ atoms form a four-spin cluster. In a separate study, we have made extensive simulations of multispin effects in a three-spin system in the presence of short T$_2^{ZQ}$ relaxation.[62] We found that these effects are reduced in the presence of short ZQ relaxation, with estimated systematic errors smaller than those introduced by the omission of CSA.

Structure Refinement of GB1. A total of 153 dipolar contacts were detected in the HBR^2 spectra. Of these, 100 distances were extracted and analyzed using the simplified two-spin model: 31 contacts were classified as intraresidue, 36 contacts corresponded to sequential spin−spin interactions, and 19 and 14 contacts were medium and long-range order interactions, respectively. Forty one contacts could not be fitted with quantitative reliability because of the lack of a statistically significant number of points. Twelve additional intermolecular interactions were also detected. The summary of all measured distances is given in the Supporting Information.

The distance constraints derived from the HBR^2 experiments were combined with 84 dihedral angles derived from TALOS analysis, subjected to a standard structure calculation using Xplor-NIH,[71] and resulted in a low-resolution structure of the protein. To improve the quality of structure, and to test the potential use of HBR^{2}W measurements for structure refinement, we collected a set of 3D (NCOCX, NCACX) and a 2D $^{13}C-^{13}C$ correlation spectra with 500 ms of proton driven spin diffusion for $^{13}C-^{13}C$ mixing. First, NCACX and NCOCX spectra were analyzed, and a total of 241 (185 distances from NCACX and 56 distances from NCOCX, excluding any overlap with the HBR^2 data) contacts have been identified from these experiments. The cross-peaks were assigned based on the consistency with the global fold derived from the HBR^{2}W data and TALOS restraints and were all classified to be in the range 2.9−7.5 Å. A number of cross-peaks detected in PDSD spectra appeared to be inconsistent with the HBR^2 template structure and were discarded. These peaks may have corresponded to the long-range relayed transfers. In general, the use of the HBR^2 template data and fairly conservative boundaries used for the
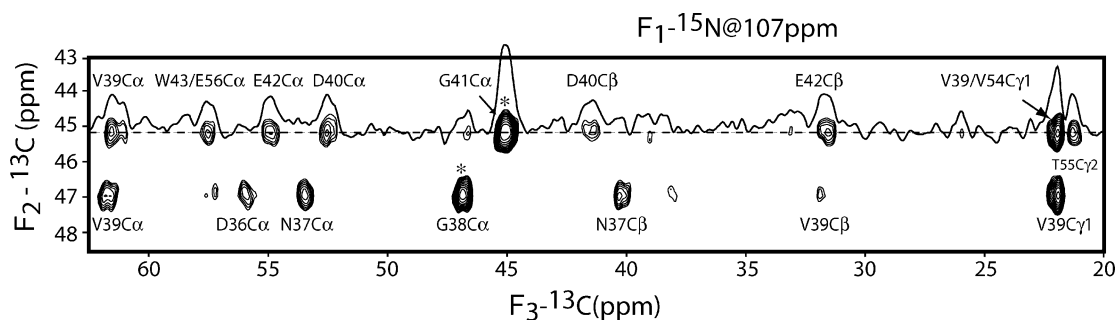
Figure 8. 2D $^{13}C-^{13}C$ plane of three-dimensional NCACX spin diffusion experiment. The NCA pseudo-diagonal peaks are indicated by asterisks. Medium (e.g., G41Cα-V39Cα, G38Cα-D36Cα) and long-range correlations (e.g., G41Cα-V39/V54γ1, G41Cα-T55γ2) are detected in the spectra. 88 real data points with an increment of 256.9 μs were collected in t_1, 400 real data points with an increment of 33.1 μs were collected in t_2, and 2560 complex points with a 11 μs dwell time were collected in t_3. The data were processed with exponential line broadening of 2.0 Hz in the F_1 dimension and the $\pi/2$-shifted square sinusoidal window function in the F_2 and F_3 dimensions.

PDSD restraints minimize the chances that the cross-peaks due to multistep magnetization transfers will be mistakenly interpreted as positive contacts between carbon spins in a spatial proximity.

A representative 2D plane of the full 3D NCACX experiment is shown in Figure 8. Although we were originally concerned that the short-range interactions would dominate the polarization transfer because of the residual dipolar truncation effects, a large number of nontrivial cross-peaks have been observed. From these two experiments, a total of 75 sequential, 116 medium, and 50 long-range correlations were obtained. These numbers do not include Cα[i]−Cα[i±1] contacts and all the restraints overlapping with HBR[2] data.

The 2D $^{13}C-^{13}C$ spin diffusion data provided an additional 186 constraints (of which 45 were long-range and 48 were medium-range contacts), many of them corresponding to long-range side chain−side chain interactions. The cross-peak assignments in the crowded 2D $^{13}C-^{13}C$ PDSD spectrum were also accomplished based on the consistency with the 3D fold derived from HBR[2] and NCOCX and NCACX PDSD measurements.

Structure Calculation. In addition to the structure calculation based on HBR[2] and TALOS constraints described previously, two more structure calculations were performed. In the first, a complete set of 568 distances (427 spin diffusion restraints and 141 intramolecular HBR[2] constraints) and 84 TALOS dihedral angle restraints was subjected to a standard structure calculation protocol starting from a linear conformer. The structure calculation was carried out using the Xplor-NIH package,[71] with a violation report threshold set to 0.2 Å. During the course of calculation trials, the following iterative procedure was performed: if distance violations were reported consistently in the family of structures, they were removed from the restraint list and another calculation was performed, until no violation greater than 0.2 Å was reported in the final calculation. Only 7 spin diffusion restraints out of a total of 568 were rejected in the whole course of the iterative calculation procedure. A family of 500 structures was calculated, and the 25 lowest energy structures were selected for subsequent structure quality analysis using the PROCHECK package.[73] 94% of backbone torsion angles were reported in the most favored region, 4% were in the additional allowed region, and one residue, Lys10 located in the turn connecting β1 and β2 strands, was found to be in
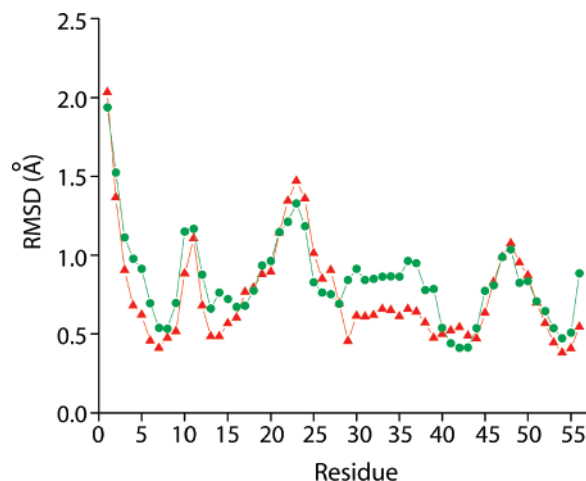
(73) Laskowski, R. A.; Rullmann, J. A. C.; MacArthur, M. W.; Kaptein, R.; Thornton, J. M. *J. Biomol. NMR* **1996**, *8*, 477−486.

Figure 9. A comparison of the backbone RMSDs for 10 lowest energy structures calculated from spin diffusion and HBR[2] data (red) and from spin diffusion and HBR[2] data set to spin diffusion limits of 2.9−7.5 Å (green).

the disallowed region. An overall backbone rmsd obtained in this calculation was 0.8 Å.

A similar structure calculation, but with HBR[2] constraints redefined to the PDSD limits of 2.9−7.5 Å, was repeated and resulted in a family of 10 lowest energy structures with a larger backbone rmsd of 0.9 Å. The results of two calculations are summarized in Figure 9, where RMSDs are compared for each residue. The improvement is localized to Lys4-Thr17 and especially Val29-Val39 fragments, where locally defined RMSDs improve by as much as 0.3−0.4 Å.

Conclusions

We have presented a new experimental approach for $^{13}C-^{13}C$ distance measurements in uniformly $^{13}C,^{15}N$ labeled proteins. The experimental pulse sequence is robust and easy to implement. Because all of the chemical shift evolution periods are recorded on nuclei that are relatively insensitive to the decoupling conditions (nitrogens, carbonyl carbons, methyl carbons), the experiment can be conducted at a low proton decoupling power without significantly sacrificing the spectral resolution.

The experiments presented in this work were conducted at a 600 MHz proton field and required only moderate spinning frequencies in the range 11.3−12.4 kHz, readily achievable in modern NMR probes. At high magnetic fields, matching the

$n = 2$ R^2 condition will require faster spinning frequencies, e.g., $17-18.6$ kHz, which are also readily available in the modern MAS probes. Thus, the experimental approach is directly extendable to higher fields, albeit the homogeneous width of the R^2 matching condition is expected to be somewhat narrower, due to more efficient averaging of $^1H-^1H$ dipolar couplings by fast MAS.

In GB1, the experiment provided accurate distances up to 5.5 Å. It should be emphasized that although the two-spin approximation employed for data analysis appeared to adequately describe the experimental data, this is so in large part because of the relatively large systematic errors associated with the omission of the CSA effects. In principle, the CSA-related errors could be reduced if the carbonyl CSA orientations were included in the iterative structure refinement, but such a procedure would necessarily require a proper analysis of the multispin processes.

An additional point of concern in quantitative analysis of HBR^{2}W curves is whether the assumption of rigid internuclear distances introduces additional systematic errors. In particular, large amplitude motions involving reorientation of the side chains, occurring on a time scale of the dipolar $^{13}C-^{13}C$ interactions or faster, are likely to affect the outcome of distance measurements. Franks et al.[65] have found that the isotropic chemical shifts and side chain cross-peak intensities in 2D SPC5[74] $^{13}C-^{13}C$ correlation spectra of GB1 are consistent with significant side chain dynamics, most notably in V21. Quantification of these motions requires separate study and is beyond the scope of this publication. A strong argument that the errors associated with the dynamic effects are smaller than those resulting from the omission of CSA is the fact that the set of distances we obtained from the HBR^{2}W and PDSD data is self-consistent.

The constraints derived from the HBR^2 experiments alone were sufficient to derive a global fold of the protein, but only at a low resolution. An optimal strategy appears to be to combine HBR^2 $^{13}C-^{13}C$ constraints with restraints derived from other experiments, for example, from PDSD or DARR experiments. In GB1, the addition of HBR^2 constraints improved the rmsd of structure for approximately 45% of the residues. We anticipate that the types of measurements presented in this work would be of greater significance in systems with extended secondary structure motifs, where only a limited number of long-range intramolecular contacts are available. In this respect, the importance of short-range accurate distance constraints has been demonstrated in amyloid fibrils.[60] The $^{13}C-^{13}C$ constraints should be complemented with other refinement techniques, including methods for the determination of dihedral angles,[36-38] as well as for $^1H-^1H$, $^{13}C-^{15}N$, and $^{15}N-^{15}N$ distances,[54,75] to be able to solve high-resolution structures for proteins not amenable to X-ray crystallography or solution NMR.

Supporting Information Available: Supplemental figures and tables, details of the iterative cross-peak assignment procedure. This material is available free of charge via the Internet at http://pubs.acs.org.

JA076658V

(74) Hohwy, M.; Rienstra, C. M.; Jaroniec, C. P.; Griffin, R. G. *J. Chem. Phys.* **1999**, *110*, 7983−7992.

(75) Reif, B.; van Rossum, B. J.; Castellani, F.; Rehbein, K.; Diehl, A.; Oschkinat, H. *J. Am. Chem. Soc.* **2003**, *125*, 1488−1489.